

Long-lived transient structure in collisionless self-gravitating systemsDavid Benhaiem,¹ Francesco Sylos Labini,^{1,2,3} and Michael Joyce⁴¹*Istituto dei Sistemi Complessi, Consiglio Nazionale delle Ricerche, Via dei Taurini 19, 00185 Roma, Italy*²*Centro Studi e Ricerche Enrico Fermi, Piazza del Viminale 1, 00184 Roma, Italy*³*INFN Unit Rome 1, Dipartimento di Fisica, Università di Roma Sapienza, Piazzale Aldo Moro 2, 00185 Roma, Italy*⁴*Laboratoire de Physique Nucléaire et de Hautes Énergies, UPMC, IN2P3, CNRS, UMR No. 7585, Sorbonne Université, 4 Place Jussieu, 75252 Paris Cedex 05, France*

(Received 25 June 2018; published 14 February 2019)

The evolution of self-gravitating systems, and long-range interacting systems more generally, from initial configurations far from dynamical equilibrium is often described as a simple two-phase process: a first phase of violent relaxation bringing it to a quasistationary state in a few dynamical times, followed by a slow adiabatic evolution driven by collisional processes. In this context the complex spatial structure evident, for example, in spiral galaxies is understood either in terms of instabilities of quasistationary states or as a result of dissipative nongravitational interactions. We illustrate here, using numerical simulations, that purely self-gravitating systems evolving from quite simple initial configurations can in fact give rise easily to structures of this kind, of which the lifetime can be large compared to the dynamical characteristic time but short compared to the collisional relaxation timescale. More specifically, for a broad range of nonspherical and nonuniform rotating initial conditions, gravitational relaxation gives rise quite generically to long-lived nonstationary structures of a rich variety, characterized by spiral-like arms, bars, and even ringlike structures in special cases. These structures are a feature of the intrinsically out-of-equilibrium nature of the system's collapse, associated with a part of the system's mass while the bulk is well virialized. They are characterized by predominantly radial motions in their outermost parts, but also incorporate an extended flattened region which rotates coherently about a well-virialized core of triaxial shape with an approximately isotropic velocity dispersion. We characterize the kinematical and dynamical properties of these complex velocity fields and we briefly discuss the possible relevance of these simple toy models to the observed structure of real galaxies, emphasizing the difference between dissipative and dissipationless disk formation.

DOI: [10.1103/PhysRevE.99.022125](https://doi.org/10.1103/PhysRevE.99.022125)**I. INTRODUCTION**

The dynamical evolution of many particles solely interacting by Newtonian gravity is a fundamental paradigmatic problem in physics, which is essential for the modeling and interpretation of astrophysical structures. The study of this problem can also be placed in the broader framework of long-range interactions, which, from the point of view of statistical mechanics, share essential features (for a review see, e.g., [1–3]). An approach based on equilibrium statistical mechanics (for the case of gravity see, e.g., [4,5]) is physically relevant to such systems only on timescales that are very long compared to the those characteristic of the mean-field dynamics driven by the collective force fields sourced by many particles and described by Vlasov equations. This dynamics leads typically to dynamical equilibria referred to variably as virial equilibria, collisionless equilibria, or quasistationary states (QSSs); we will adopt the latter term here. These states are interpreted as stationary states of the appropriate Vlasov equation. Such states can also manifest instabilities leading to further evolution, giving rise, for example, to changes in symmetry (through radial orbit instability) and/or to the development of complex spatial structure (through, e.g., spiral wave instabilities). On longer timescales, diverging in particle number when expressed in terms of the dynamical time

characteristic of the mean-field time and described theoretically by a broader framework than the Vlasov equations incorporating collisional terms, such systems then typically evolve adiabatically through a QSS, finally evolving to thermal equilibrium if such a state is well defined (see, e.g., [1,6–11].)

For the case of gravity in three dimensions, numerical studies indicate (see, e.g., [12] and references therein) that collisional evolution is driven primarily by two-body collisions on a timescale of the order of $\tau_{\text{coll}} \sim [N/\ln(N)]\tau_{\text{dyn}}$, where $\tau_{\text{dyn}} \sim 1/\sqrt{G\rho}$ (where ρ is the system's average density), as originally argued by [13]. In most astrophysical systems the timescale for such relaxation is this much longer than the Hubble time and their dynamics, on relevant timescales, is thus expected to be accurately described by the collisionless (mean-field) dynamics. The framework for the study of stellar and galactic dynamics (see, e.g., [14]) is thus that of the collisionless Boltzmann equation (i.e., the Vlasov equation coupled to the Poisson equation). Because of the extremely long timescale of collisional relaxation, the assumption of stationarity is often used as a working hypothesis for studying the structure of galaxies, with possible secular evolution through collisionless dynamics. In this context the striking spatial structuration of galaxies, most evidently spiral structure, has been described analytically in terms of instabilities of such

QSSs (see, e.g., [15] and references therein). With modern numerical studies of galaxy formation (see, e.g., [16–24] and references therein) there has been extensive study of the origin of such structure, but an essential role in its generation is then played by dissipative nongravitational processes. In this paper we report results showing that structures of this kind can arise purely within the restricted framework of self-gravitating systems. Further, these structures, despite the fact that they are generated by a collisionless dynamics, are the result of a far-from-equilibrium state which persists for times which are very long compared to the dynamical time on which the initial approximate virialization of the system occurs.

To study these transient configurations we evolve numerically, using gravitational N -body simulations, a set of toy models; this allows us to understand the basic physical processes which give rise to such out-of-equilibrium structures. The relaxation of isolated self-gravitating systems from simple initial conditions (ICs), of the kind we consider here, has been extensively studied in numerical simulations over several decades (see, e.g., [25–32]). The focus of such studies has almost exclusively been on the formation and properties of the virialized structures which are very efficiently produced by the collapse’s dynamics. In particular, in the context of the theory of galaxy formation, there was much interest in the capacity of such ICs to produce structures resembling elliptical galaxies. The focus of our study here is instead on an aspect of these systems which has been overlooked: the production of rich transient structures from the small but non-negligible fraction of loosely bound and ejected mass which is very generically also produced by the relaxation process [33–35]. This phenomenon is of basic theoretical interest and potentially of considerable relevance to understanding astrophysical structures. In a recent article [36], we have shown that, starting from a specific class of simple idealized IC, uniform rotating ellipsoidal configurations, the relaxation of the system under its self-gravity typically leads to extended transient structures resembling qualitatively that of the outer parts of spiral galaxies. In the study reported in this paper, we investigate a much broader range of ICs, with a greater range of particle number, and whether these phenomena occur more generically. Our principle finding is that the generation of such structures, which, although transient in nature, may be very long-lived (in units of the system’s characteristic dynamical time), is indeed a quite robust and generic feature of violently relaxing systems. Further, the morphologies of the structures produced are even more rich and diverse than we had anticipated.

The spiral-like structures generated far out of equilibrium in the systems we study arise in a manner very different from that usually envisaged in the modeling of such structures in the astrophysical literature. The mechanisms proposed are perturbative in nature, envisaging the spiral-like structure as the result of instability of an equilibrium disk configuration (see, e.g., [14,15]). In addition, it is well known that the formation of flat disklike configurations can be obtained with simulations of collapsing spheroids where, in addition to gravity, the dissipative effects of several astrophysical processes are taken into account (see, e.g., [16–22] and references therein). Indeed, in this context, an indispensable element for the appearance of such structures is the inclusion of gas

with a dissipative dynamics (e.g., cooling). The principle motivation for including this dynamics was initially to allow such structures to be produced. The central finding of our study, in contrast, is that disklike configurations with transient spiral arms and with bars and/or rings may be produced by a purely (i.e., nondissipative) gravitational dynamics. We will discuss below in further detail this essential difference with respect to previous works in the literature. We also stress the peculiar features of the complex velocity fields generated by the gravitational dynamics we have investigated, which are different from the structures of this kind generated by dissipative dynamics. Indeed, while in the latter case the velocity fields are essentially dominated by rotational motions, in the former case these show different regimes and are essentially radial in the systems’ outermost regions.

The article is organized as follows. In Sec. II we describe the implementation of the numerical simulations, discussing our choice of numerical parameters, ICs, and the specific quantities we have measured. In Sec. III we present our results, focusing in particular on the spiral-like bars and rings transients produced. We describe in considerable detail the mechanism producing them, which varies in detail from one kind of IC to the other. We turn in Sec. IV to a brief discussion of the possible relevance to real galactic structures of our simple models. The differences between dissipative and nondissipative dynamics in the process of the formation of a disklike structure are discussed in Sec. V. Finally, in Sec. VI we summarize our findings and outline some of the many further questions raised by them.

II. NUMERICAL SIMULATIONS

Our numerical experiments consist of molecular dynamics simulations of a Hamiltonian system of N -point particles in an infinite (three-dimensional) domain, interacting by a pair potential ϕ which is that of Newtonian gravity with a short-distance regularization. They have been performed using the publicly available (and widely used) code GADGET-2 [37], in the appropriate version (nonexpanding universe, with open boundary conditions). The regularization of the potential, the so-called gravitational softening, in this code is implemented by solving the Poisson equation for spherical continuous clouds, with compact support of characteristic radius ε (and total mass equal to that of the particle). The force thus takes exactly its Newtonian value at separations greater than ε . The functional form of the regularized potential for $r < \varepsilon$, of which the exact expression can be found in [37], is a cubic spline interpolating between the exact Newtonian potential at $r = \varepsilon$ and a constant value at $r = 0$, with vanishing gravitational force at this point.

A. Precision and softening

For simulations of the dynamics from the IC we consider, which give rise typically to very significant contraction of the system, leading to very high densities and short characteristic timescales, the choice of the force softening length and numerical parameters controlling the accuracy of the time stepping and force calculation requires particular care. We have performed simulations, which we call low precision (LP),

with the numerical parameters of the code set at the values suggested by the GADGET-2 user guide [38]. We monitored the total energy and found that these runs typically conserve it to within about 0.5%. We then also ran high precision (HP) simulations using values of the relevant parameters which lead to energy conservation to within one part in 10^5 .¹ We also monitored conservation of total linear and angular momentum conservation and observed similar results.

We have run both LP (with N in the range $[10^4, 5 \times 10^5]$) and HP (with N in the range 10^6) simulations of realizations of our IC (described in detail below) and found no apparent significant differences for the macroscopic quantities which we study. In what follows we will report only results for LP simulations, which likewise give results completely consistent with the lower N simulations at HP and LP. Thus it appears that our results are N independent, and represent those of an $N \rightarrow \infty$ limit. However, as we discuss further below, such a conclusion should be treated with caution.

Our default value of the force softening length (the code's parameter ε), as well as that used in the specific simulations reported below, is 10^{-3} in the units of length we define further below. In practice this means it is 10^{-3} of the smallest characteristic length in the IC (e.g., the shortest semiprincipal axis in the case of an initial ellipsoid) and is such that it is always considerably smaller than the typical size of the system when it is most contracted. We have also performed extensive tests to control the effect of varying the force-softening parameter and found that we indeed obtain very stable results, provided this condition is respected on the comparison of ε and the minimal size reached by the whole structure during the collapse.

We have also run some test simulations in which the particles have two different masses. Specifically, in a reference simulation in which all the particles have mass m , we have resampled randomly with particles of mass $\alpha \times m$ and m/α , with $\alpha = 2, 5, 10$, determining their number so that the total mass is fixed. We then studied the spatial and velocity properties of the two species separately and found them to be in good agreement both with one another and with the properties found in the original single mass simulation of the IC. This provides strong evidence that the dynamics producing the distributions we have described are indeed representative of the mean-field (or collisionless) dynamics of the continuum IC we have sampled. Indeed, this is consistent with what one would expect as, even for the longest times we simulate (at most 200 dynamical times), collisional two-body effects would be expected to be negligible for the particle numbers we consider even in the virialized core of the system.

B. Initial conditions

We wish to study the evolution of self-gravitating N -body systems starting from ICs which are sampled from spatial mass distributions which break rotational symmetry and also mass distributions which are nonuniform (i.e., for which the

mass density is not constant in the compact region where it is nonzero). Clearly, the space of parameters that describe a generic IC of this type is infinite. We have chosen three very simple few-parameter families of such ICs. In order of increasing complexity, we consider mass distributions which are (i) uniform ellipsoids, (ii) uniform ellipsoids with a central spherical region of higher density, and (iii) a collection of uniform spheres of varying radii with centers randomly placed in a spherical region. For the initial velocities we consider only two very simple cases: coherent rigid-body-type rotation of the whole structure and, in a few cases only, some additional random uncorrelated motion. The precise details of our choices for how the different ICs are then parametrized are given below.

With these choices of ICs we aim to single out the effect of the initial shape of an isolated mass distribution on its collapse and subsequent evolution. This aspect appears to have been largely overlooked in the literature, which has focused instead mostly on the effect of internal correlations between density fluctuations, for the case of a spherical cloud [16–22]. As we discuss below, one of our main results is that the spherical ICs represent a very peculiar and pathological case that gives rise to the dynamics that suppresses a common characteristic feature of the gravitational collapse of isolated overdensities: the formation of a disklike structure with spiral-type arms that occurs when the ICs significantly break spherical symmetry.

1. Uniform ellipsoidal clouds

For this class of systems the particles are (i) randomly distributed, without correlation, with uniform probability inside an ellipsoid, and (ii) given a coherent rigid-body rotation about the shortest semiprincipal axis. The three parameters which we choose to characterize them are the ratios a_1/a_3 and a_2/a_3 of the two longer semiprincipal axes ($a_1 \geq a_2$) to the shortest one a_3 and the virial ratio associated with the rotation

$$b_{\text{rot}} = \frac{2K_{\text{rot}}}{W_0}, \quad (1)$$

where K_{rot} is the kinetic energy of the rotational motion and W_0 is the initial gravitational potential energy. As mentioned above, we have considered some numerical experiments in which we add a random motion in addition to the coherent rotational one. The amplitude of this motion has been taken to be a fraction of the order of 10%–20% of the rotational one. We have not found any significant difference on a macroscopic scale, but the transient features like the spiral arms are indeed more diffuse when random motions have the highest amplitude we have tested.

We have performed simulations for a large variety of prolate (i.e., $a_1 > a_2 = a_3$), oblate (i.e., $a_1 = a_2 > a_3$), and triaxial (i.e., $a_1 > a_2 > a_3$) shapes, as well as the special case when the cloud is spherical (and thus rotational symmetry is broken only by the finite- N Poissonian fluctuations). We have explored the range of values defined by the ratio a_1/a_3 , $a_2/a_3 \in [0.05, 2]$. For the velocities we have explored the range $b_{\text{rot}} \in [-1, -0.05]$. We report in detail results for just two representative cases A1 and A2 for which the parameter values are given in Table I. We report also the value of the

¹Specifically, the parameter `ErrTolTheta` is 10^{-10} for HP compared to 0.7 for LP, while `ErrTolForceAcc` is 10^{-10} for HP and 5×10^{-4} for LP.

TABLE I. Values of the relevant parameters (see the text) for the specific simulations we report here.

Simulation	$\frac{a_1}{a_3}$	$\frac{a_2}{a_3}$	$\frac{R}{a_3}$	$ b_{\text{rot}} $	$\frac{M_e}{M_s}$	N_c	$\frac{\ell_c}{\Lambda_c}$	λ
A1	2	1		0.2				0.19
A2	2	1.25		1.0				0.30
B1	1.5	1	0.1	0.25	1			0.12
B1a	1.5	1	0.01	0.25	1			0.29
B2	1.5	1.5	0.1	0.50	3			0.29
C1				1		5	0.5	0.28
C2				0.8		10	0.5	0.17

so-called spin parameter as defined in [39,40],

$$\lambda = \frac{J|E|^{1/2}}{GM^{5/2}}, \quad (2)$$

where J is the total angular momentum of the system, E the binding energy, M the total mass, and G Newton's constant. This parameter is widely used in the astrophysical context when characterizing the angular momentum of astrophysical systems (see also, e.g., [41,42]). It simply provides a dimensionless measure of the angular momentum in the natural units of a self-gravitating system (given by dimensional analysis by the combination of $GM^{5/2}/E^{1/2}$). It thus provides an indication of the degree of rotational support of a self-gravitating system provided by its angular momentum.

2. Nonuniform ellipsoidal clouds

In this class of systems we consider a coherently rotating ellipsoidal configuration exactly as described above, but then modify it in a spherical region around its center, ascribing a different number (and thus mass density) of uniformly distributed particles, and only random uncorrelated velocities, sampled uniformly in velocity space up to a maximal magnitude.

We consider only the case that the kinetic energy K_s of the particles in the spherical region is such that $2K_s = -W_s$, where W_s is their potential energy, i.e., this central region is initially approximately virialized. The initial conditions are thus chosen to probe the dynamics of the collapse of a rotating ellipsoidal cloud which already has a smaller virialized structure inside it. There are then five parameters characterizing this family of ICs, which we choose to be a_1/a_3 , a_2/a_3 , R/a_3 (where a_i are again the lengths of the semiprincipal axes and R is the radius of the sphere), the ratio M_e/M_s of mass (i.e., particle densities) in the ellipsoidal region to that in the sphere, and the ratio b_{rot} as given in (1), with W_0 the total potential energy of the configuration of the ellipsoid alone.

We have considered simulations in which $b_{\text{rot}} \in [-1, -0.1]$, which means that in almost all cases all particles are initially bound. For the other parameters we have explored $a_1/a_3, a_2/a_3 \in [0.05, 2]$, $R/a_3 \in [0.01, 0.1]$, and $M_e/M_s \in [1/3, 3]$.

We note that the characteristic time for collapse of the rotating cloud, in units of the dynamical time of the sphere, is $\sim (a_3/R)^{3/2} (M_s/M_e)^{1/2}$. Thus we explore the range in which this ratio is between about 10–30. We report in detail results

for just three representative cases B1, B1a, and B2, for which the parameter values are given in Table I.

3. Nonspherical and nonuniform clouds

The third class of models consists of mass distributions which still rotate coherently, but in which rotational symmetry is broken in a more random and less idealized manner. Specifically, we choose N_c points randomly with uniform probability in a sphere of radius R_0 . Taking each of these N_c points as centers, we distribute randomly N_p points in spheres of radius ℓ_c centered on them. We calculate the moment of inertia tensor and use it to determine the direction of the principal axis with the largest eigenvalue. We give a coherent rigid-body rotation to the whole cloud about this axis.

For a given total particle number, this is thus a three-parameter family of configurations. We take these parameters to be N_c , ℓ_c/Λ_c , and b_{rot} , where the latter is given again by Eq. (1) with W_0 the total initial potential energy. Here Λ_c is the mean distance between neighboring clouds $\Lambda_c \approx 0.55(4\pi R_0^3/3N_c)^{1/3}$ and the parameter ℓ_c/Λ_c thus characterizes the degree of overlap of the individual clouds. We are in practice interested in values not so different from unity so that the initial density fluctuations are not so large and there is a global collapse of the whole structure (rather than separate collapses for the substructures and the whole structure). We have studied the range of parameters $N_c \in [3, 50]$, $\eta = \ell_c/\Lambda_c \in [0.1, 2]$, and $b_{\text{rot}} \in [-1, -0.1]$. We again report results for just two cases C1 and C2, specified in Table I, whose features are representative of this class of models.

It is important to note that our random sampling with a finite number N of particles introduces mass density fluctuations, which are additional to those intrinsic to our continuum IC. Such density fluctuations can of course play a role in the dynamics, and as their amplitude is N dependent (with $\frac{\delta\rho}{\rho} \sim 1/\sqrt{N}$), one might expect this to induce potentially an N dependence in our results even for macroscopic results. However, as detailed above, the parameters of our IC are in fact chosen so that $\frac{\delta\rho}{\rho} \sim 1$, so one might expect the finite- N fluctuations to be negligible. We discuss in more detail finite- N effects and the problem of taking the continuum limit in Sec. III K.

As noted above, this is indeed consistent with our numerical findings over a range of N between 10^4 and 10^6 . For this reason we present in the paper only results for the case $N = 10^6$ and do not discuss any further the role of N in our results. Nevertheless, we caution that it is quite possible that the physical processes we simulate might have subtle dependences on N which do not show up clearly in the range we have simulated. Notably, as illustrated by the study in [43] of the special case of spherical ICs, such dependences may arise because the finite- N fluctuations break symmetries of our continuum ICs.

C. Physical quantities measured

A useful basic quantity to monitor the global evolution of the system is the gravitational radius defined by

$$R^g(t) = \frac{GM_b(t)^2}{|W_b(t)|}, \quad (3)$$

where $W_b(t)$ is the gravitational potential energy of the bound particles and $M_b(t) \leq mN$ is their mass. To characterize the system's shape we compute the three eigenvalues λ_i (with $i = 1, 2, 3$) of its inertia tensor, which, in the case of an ellipsoid, are related to the lengths a_i of the three semiprincipal axes by

$$\lambda_i = \frac{1}{3}M_b(a_j^2 + a_k^2), \quad (4)$$

where $i \neq j \neq k$ and $i, j, k, = 1, 2, 3$. It follows that $\lambda_1 \leq \lambda_2 \leq \lambda_3$. It is standard then to introduce three different combinations of the λ_i : the flatness parameter

$$\iota = \frac{\lambda_3}{\lambda_1} - 1, \quad (5)$$

the triaxiality index

$$\tau = \frac{\lambda_3 - \lambda_2}{\lambda_3 - \lambda_1}, \quad (6)$$

and the disk parameter

$$\phi = \frac{\lambda_3 - \lambda_1}{\lambda_2 + \lambda_1}. \quad (7)$$

These parameters allow one to distinguish not only between different types of ellipsoids (e.g., prolate, oblate, and triaxial) but also between other shapes (i.e., bars vs disks). For instance, a sphere has $(0, -, 0)$, a disk $(1, 0, 0.5)$, and a narrow cylinder (i.e., a bar) $(\gg 1, 1, \approx 1)$.

In addition to the radial component of a particle's velocity \vec{v} ,

$$v_r = \frac{\vec{v} \cdot \vec{r}}{|\vec{r}|}, \quad (8)$$

we define the vectorial transverse velocity as

$$\vec{v}_t(r) = \frac{\vec{r} \times \vec{v}(r)}{|\vec{r}|}, \quad (9)$$

i.e., the vector whose magnitude is that of the nonradial component of the velocity, but oriented parallel to the particle's angular momentum relative to the origin. We will denote the average of a quantity in a spherical shell about radius r by $\langle \dots \rangle$. Coherent rotation of all the particles in the shell about the same axis then corresponds to $\langle |\vec{v}_t| \rangle = |\langle \vec{v}_t \rangle|$. Furthermore, we consider the anisotropy parameter

$$\beta(r) = 1 - \frac{\langle v_t^2 \rangle}{2\langle v_r^2 \rangle}, \quad (10)$$

where $\langle v_t^2 \rangle$ and $\langle v_r^2 \rangle$ are, respectively, the average square value of the transversal and radial velocities. The anisotropy parameter has the following limiting behaviors: $\beta \rightarrow 0$ for an isotropic velocity distribution and $\beta \rightarrow 1$ when $\langle v_t^2 \rangle \ll 2\langle v_r^2 \rangle$, i.e., when the motion is predominately radial.

To characterize the kinematics further, we also consider the different components of the radial acceleration, which can be decomposed as

$$a_r = \dot{v}_r - \frac{v_t^2}{r} = \dot{v}_r - a_c, \quad (11)$$

where a_c is the magnitude of the centripetal acceleration associated with the transverse component of the velocity. To

quantify in a simple manner the degree of circular vs radial motion, we will consider the ratio

$$\zeta = \frac{\langle \dot{v}_r \rangle}{\langle a_r \rangle}. \quad (12)$$

When particles' motion is purely circular we thus have $\zeta = 0$, while if it is purely radial we have $\zeta = 1$; thus ζ captures different properties of the velocity field than β , although they both tend to unity when the motion is purely radial.

III. RESULTS

The phenomenology of the gravitational collapse of the IC we study is, in many respects, very similar to that of nonrotating isolated clouds discussed at length in previous works. We first summarize these behaviors and in particular recall the mechanism by which particles may gain enough energy even to be ejected from the system. We then subsequently focus on the features of the evolving system which are specifically associated with the initial rotational motion and in particular the emergence of long-lived spiral-like structure as well as transient bars and/or rings in the spatial configuration. We recall that all the results presented explicitly in the article are for simulations with $N = 10^6$ particles, but that all the quantities considered have shown no apparent N dependence for simulations of the same IC with N ranging from 10^4 to 5×10^5 . As noted above, this corresponds to there being no apparent dependence on the fluctuations associated with the particle sampling of the continuous mass distributions characterizing the initial conditions.

A. Units

As the unit of length we take $a_3 = 1$ for our first two families of ICs and $R_0 = 1$ for the third one. As the unit of time we then take

$$\tau_d = \sqrt{\frac{\pi^2}{8GM}}, \quad (13)$$

i.e., the characteristic time for the collapse of a sphere of radius unity (where M is the total mass of the system). Finally, particle energies will be given in units of GMm , where m is the particle mass (and $M = Nm$).

B. Collapse and reexpansion

Figure 1(a) shows the evolution of the gravitational radius (3) for three different initial conditions, which show the largest and the smallest variation among the ones we have selected. In the case of A1 and C1 the system, which is initially far from equilibrium, contracts globally, reaching a minimum on a timescale of order τ_d ($\approx 10\tau_d$ for the case of B1 because of the lower density of the external ellipsoid), then it reexpands, and, after a number of damped oscillations which varies, rapidly settles down to a fairly stable value. A similar behavior is manifested by the virial ratio [Fig. 1(b)] and thus the stabilization of R_g reflects the relaxation of the system to a state close to virial equilibrium. As we will see below, this inference is only approximately true, as a small fraction of the mass remains in a time-dependent configuration on

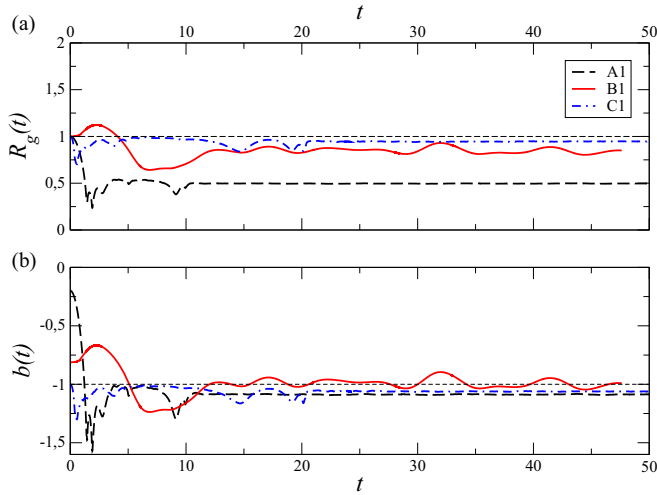


FIG. 1. (a) Gravitational radius as a function of time for different simulations. (b) Global virial ratio.

much longer timescales. Indeed, it is this fraction of the mass distribution which we will discuss at length below.

For the cases of A1 and C1 a fraction of the mass is ejected after the collapse, and as a result the global virial ratio stabilizes around a value smaller than -1 ; in the case of B1 the collapse is less violent and there is no mass ejected. We note that for B1 and C1, like all other simulations of these classes, the gravitational radius is reduced by a smaller factor than for the case of homogeneous ellipsoids. Compared to this case, the fluctuations of the gravitational field generated are thus much weaker.

C. Particle energies distributions before and after collapse

Figure 2 shows the distribution $P(E)$ of particle energies E at two different times in the same three simulations as in Fig. 1. Plotting these distributions at longer times than the last one shown, we find no noticeable evolution, i.e.,

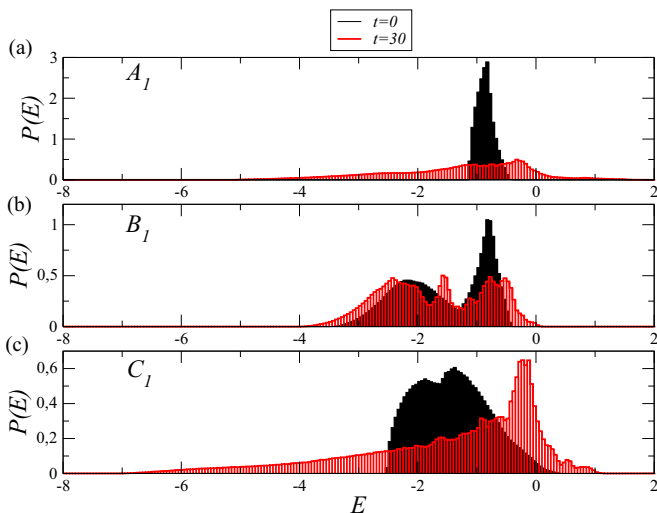


FIG. 2. Energy distribution at $t = 0$ and $t = 30$ for simulations (a) A1, (b) B1, and (c) C1 at different times (see the legend).

these distributions represent well in principle a final stationary distribution. We see that their qualitative behavior divides them clearly as in Fig. 1: In the cold simulation A1, the change in the energy distribution as a result of the dynamics is much more marked, with (i) a much more widely spread energy distribution compared to that in B1 and C1 and (ii) a significant fraction of the mass with positive energy, while there is a much smaller fraction of (or even no) such particles in the other cases. In the case of B1 there is a small but non-negligible evolution of the particle energy distribution, while C1 represents an intermediate case with respect to A1 and B1.

The correlation between the behavior in Figs. 1 and 2 is simple to understand: Changes in particle energy are driven by the variation of the gravitational field and this is much more violent in the cold cases. In the warmer case the variation of the field is relatively gentle and mixing in phase space has time to play a greater role in the relaxation process. Nevertheless, as we will see, the generation of even a small number of particles with positive energy or indeed a significant fraction of bound mass with energy close to zero is sufficient to produce a considerable and nontrivial evolution in configuration space.

Let us recall another relevant feature of these energy changes, which was shown in previous studies of ICs without rotation [33,34]: The particles which have a large energy gain, and which thus constitute predominantly both the unbound and loosely bound mass, are those which lie initially in the outer part of the structure. In the spherical case, these are the particles initially in the outer shells, and in the ellipsoidal case, these are the particles which are at large radii and close to the longest semiprincipal axis.

The reason for this correlation between the energy gain or loss and particle initial position is related to the times at which particles first pass through the center of the structure: Particles which pass through the center after the bulk of the particles experience the intense gravitational field which changes their energy at a time when it is weakening, simply because the bulk of mass generating it is already reexpanding. Such particles thus fall into a potential which is deeper than the one they subsequently climb out of and they thus have a greater net boost of their energy. In the ellipsoidal case it is quite evident why the initially outermost particles arrive late: In the evolution from such an initial condition, collapse occurs first along the shortest axis and last along the longest axis [44]. In the quasispherical case the reason for the average late arrival of particles in the outermost shells is more subtle as it is due to a boundary effect: Particles near the boundary experience a lower average density and thus have a longer fall time (see [33] for a detailed discussion).

D. Mean density profiles

Figure 3 shows the mean density averaged in radial shells of equal logarithmic thickness $\Delta[\ln(r)]$ as a function of radius for the same simulations as in Figs. 1 and 2.² We again obtain

²We take as the center the particle which has the lowest gravitational potential. Note that we will use the same radial binning everywhere below when we compute averages.

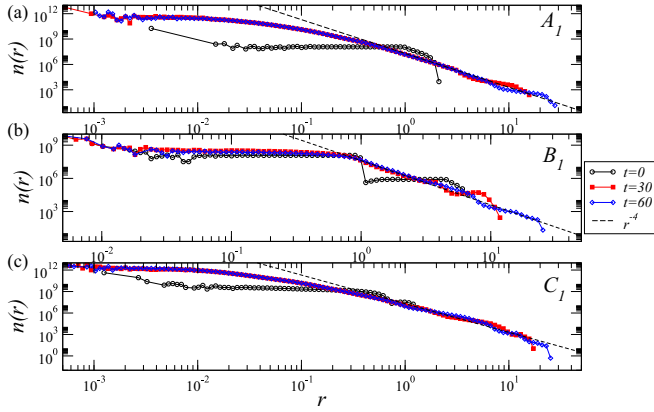


FIG. 3. Density profile for simulations (a) A1, (b) B1, and (c) C1 at different times (see the legend). The solid line corresponds to a decrease proportional to r^{-4} .

results very similar to that for nonrotating ICs, with cold ICs producing (i) a more compact core than the warmer ICs and (ii) a characteristic $1/r^4$ decay of the density at large radii. As discussed, for example, in [34], this latter behavior is associated with the very loosely bound particles on highly radial orbits and can be explained in a simple manner by considering that the outermost particles move approximately in a central and stationary potential. In these plots the system appears to settle down to a stationary form on the same timescales as inferred from the plots in Figs. 1 and 2 (and which are slightly longer for the warm cases). We can just make out the signature of some continuing evolution at the largest radii. It is this which we now focus on.

E. Nonstationary features at longer times

We consider here the nonstationary features of the mass distribution at longer times, of which the very nontrivial distinctive space and velocity structure is a result of the initial rotation of the IC. In space this can be seen very clearly in the (linear scale) snapshots of the evolving spatial configurations projected on the plane orthogonal to the initial axis of rotation of the IC, shown in Fig. 4. We focus first on how to quantify this nonstationary evolution which shows the features common to all the different ICs and then discuss subsequently the genesis of the large variety of different forms which are evident.

Figure 5 shows the particle energies averaged in shells as a function of radius for the same three simulations as in Figs. 1–3 and for two different times. In all cases, the nonstationarity is now clearly visible in the propagation to larger radii of the outermost mass, both loosely bound and unbound. This nonstationarity is essentially a consequence of the fact that the mass in this energy range has a characteristic time for virialization with the rest of the mass, which diverges as $E \rightarrow 0$ from below; to a first approximation the potential that is moved is central and stationary, with an associated Keplerian period $\tau \sim 1/(-E)^{3/2}$.

Figure 5 shows clearly that the structure can be divided into an inner stationary part and an outer nonstationary part. Examination of the properties in velocity space, illustrated in

Figs. 6–8, show that a further refinement into three distinct regions is warranted. (i) For $r < R_1$ and $\beta(r) \approx 0$, corresponding to an isotropic velocity dispersion, there is neither net radial flow nor net rotation (i.e., both $\langle v_r \rangle \approx 0$ and $|\langle \vec{v}_t \rangle| \approx 0$). This part of the distribution is the virialized core showing the approximately flat density profile discussed above.

(ii) For $R_1 \leq r \leq R_2$, there is no net radial flow (i.e., $\langle v_r \rangle \approx 0$), but there is a significant net rotation. Indeed, $|\langle \vec{v}_t \rangle|$ grows monotonically as a function of radius until it reaches a value where it is comparable to $\langle |\vec{v}_t| \rangle$, and this remains so as both quantities slowly decline over the radii up to R_2 . This latter scale is defined such that $\langle v_r \rangle > |\langle \vec{v}_t \rangle|$ for $r > R_2$. Thus the rotational motion grows until it is close to a completely coherent one around a single axis. Correspondingly, ζ is much smaller than unity as \dot{v}_r is small compared to a_c ; this region corresponds to the flattened part of the distribution where rotational motions dominate.

(iii) For $r > R_2$, net outward radial motion dominates [i.e., $\langle v_r \rangle > |\langle \vec{v}_t \rangle| \approx 0$, $\beta \rightarrow 1$, and $\zeta \rightarrow 1$ (as $a_r \approx \dot{v}_r$)] and the subdominant transversal component of the velocity decays monotonically towards zero. We note that in B1 this region is negligible as there is almost no ejected mass.

The scale R_1 does not evolve significantly with time, corresponding to the stationarity of the region inside it. The scale R_2 , which corresponds approximately to the transition from bound to unbound mass, increases monotonically with time. Indeed, the mass distribution in both the outer part of the central region and the entire outer region is manifestly nonstationary on these long timescales and remains so for arbitrarily long times.

A comparison of Fig. 4 with Figs. 6–8 shows a rather interesting property of this class of models: The more the shape of the structure formed after the collapse deviates from axisymmetry, the larger the radial velocity is at large distance from its center. In addition, we stress that Figs. 6–8 show the average components of the velocity in spherical shells, while the actual velocity fields are characterized by large anisotropies; most notably, the amplitude of the radial velocity is correlated with the semimajor axis. These features must be considered when comparing results of this class of simulations with observations (see Sec. VI).

F. Emergence and evolution of spiral structure

Detailed study of the temporal evolution of the configurations confirms that the mechanism for generation of the spiral-like structure evident in Fig. 4 is indeed the strong injection of energy given to particles which pass through the center of the system just after the time of the maximal compression. This gives these particles a significant radial component of their motion added to the initial rotational motion. The radial distance these particles subsequently travel, once they are outside the core, because of approximate conservation of angular momentum, is correlated with the angle they move through: Particles which have larger radial velocities initially thus trail behind particles with smaller radial velocities. For this process to generate a spiral-like structure, the only necessary additional ingredient is that the distribution of the directions of motion of these particles is anisotropic. This is indeed the case starting from these ICs. As we have discussed

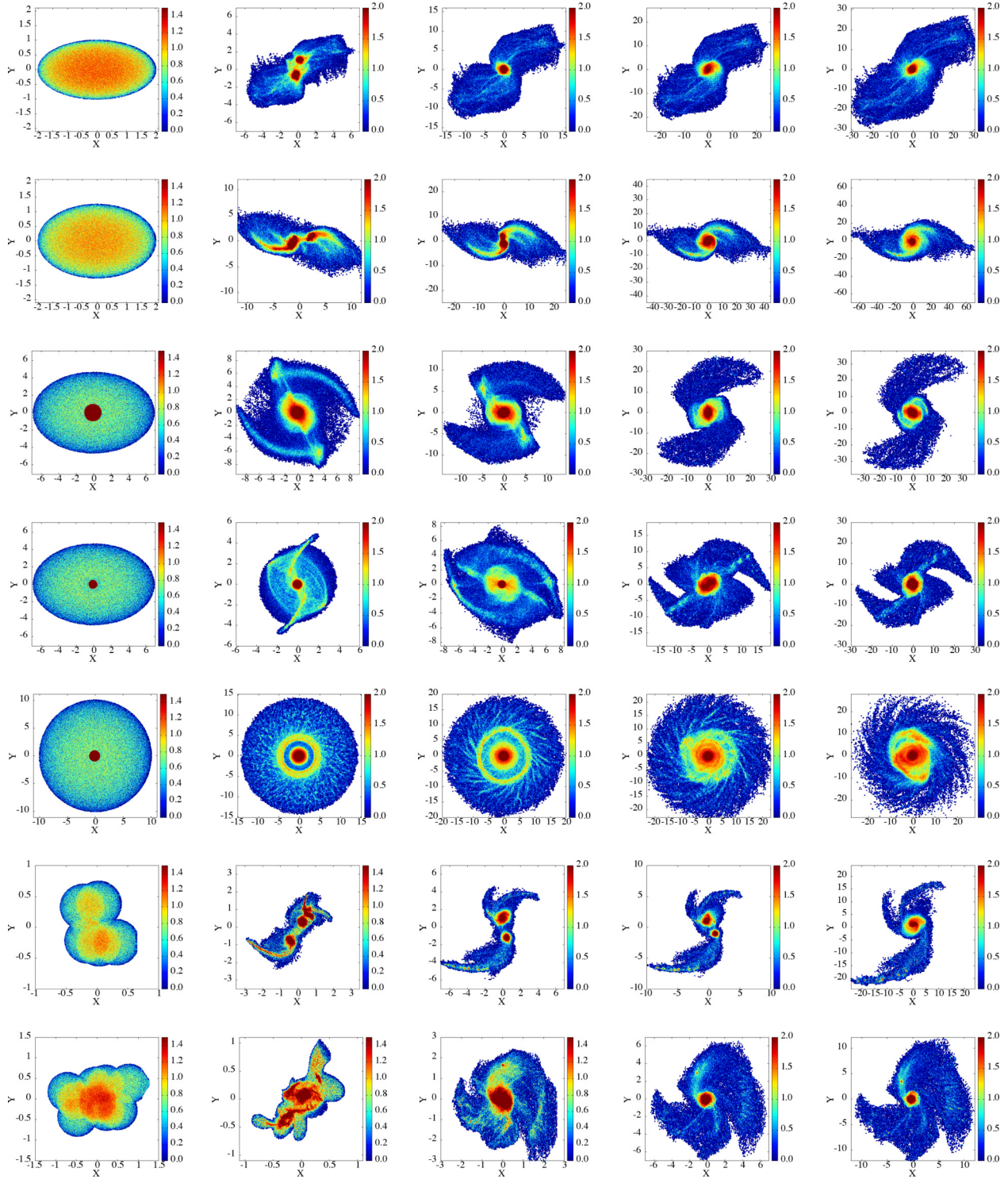


FIG. 4. Density map of several snapshots of the different simulations at the indicated times. The rows, from top to bottom, are for A1, A2, B, B1a, B2, C1, and C2. The columns, from left to right, are for $t = 0$, $t = 2\tau_{\max}$, $t = 5\tau_{\max}$, $t = 10\tau_{\max}$, and $t = 20\tau_{\max}$, where τ_{\max} is the time, determined approximately in each numerical simulation, at which the gravitational potential reaches its maximum value, which corresponds to an estimate of when the system reaches its greatest contraction. The color code is logarithmic in the density. The particle positions are projected on the plane orthogonal to the axis of initial rotation and the direction of this initial rotation is counterclockwise in these plots.

above, as for cold nonrotating ICs, the particles which gain energy are those which lie farthest from the origin initially. In the case of an ellipsoid, the radial motion arising from the energy injection is thus preferentially correlated with the

longest semiprincipal axis. Asymptotically, the motion of the particles with positive energy, which are farthest out, becomes purely ballistic and radial. As a result, the spiral-like structure is frozen and stretches more and more. Nevertheless, this

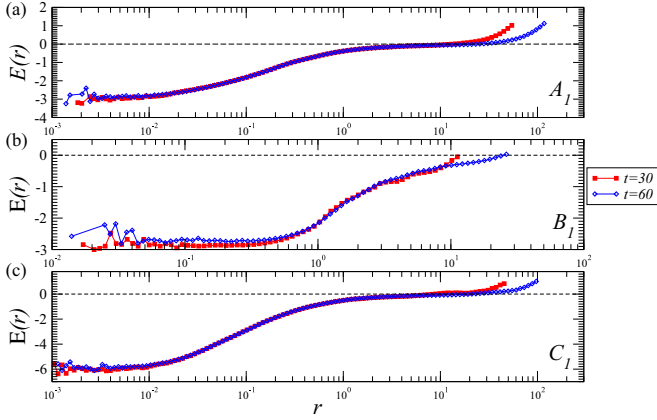


FIG. 5. Energy profile for simulations (a) A1, (b) B1, and (c) C1 at different times (see the legend).

intrinsic nonaxisymmetry of the disk is typically not yet so marked even at the quite long times we show in our plots.

We consider now in more detail the different forms arising from the range of ICs that we have selected. We recall that the first two simulations A1 and A2 in Fig. 4 show the evolution of two prolate ellipsoids (see Table I). In both cases the collapse is quite violent, with the system undergoing a very strong contraction. This leads to the production of a significant fraction (about 10%) of positive-energy particles. The collapse of most of the mass occurs along the direction of the initially shortest semiprincipal axis, while the subsequent marked expansion of the system is along the direction of the longest semiprincipal axis.

Simulation B1 shows a very similar morphology, but the spiral-like arms are markedly more wound up than in A1 and A2. Nevertheless, the basic process leading to the formation of this structure is essentially the same, with an anisotropic energy injection correlated with the axis along which particles arrive latest. This difference in the winding in particular is a direct result of a much less violent collapse, in which only a relatively small fraction of the total mass participates. As a result, the radial velocities injected into particles along the longest semiprincipal axis are smaller and the particles thus travel a smaller radial distance as they rotate with their initial rotational motion. The outer shells initially collapse toward the center in a contraction which is fastest along the shortest semiaxis. This contraction enhances the initial anisotropy of the system, which also leads to a transient bar structure, which we discuss in greater detail below.

In B1a, in which the core is a factor 10 less extended than in B1, the evolution is very similar, except for the morphological details of the bar and spiral arms. This test shows that the precise morphology of the system formed after the collapse depends sensitively on the features of the IC.

The simulation B2 likewise is characterized by a very anisotropic collapse, but as it is an oblate ellipsoid, the contraction occurs along the direction of the shortest semiprincipal axis, and approximate symmetry about this axis is maintained. The contraction does not change the particle energy distribution very significantly, but is enough to give to some particles a radial velocity component directed outward. In

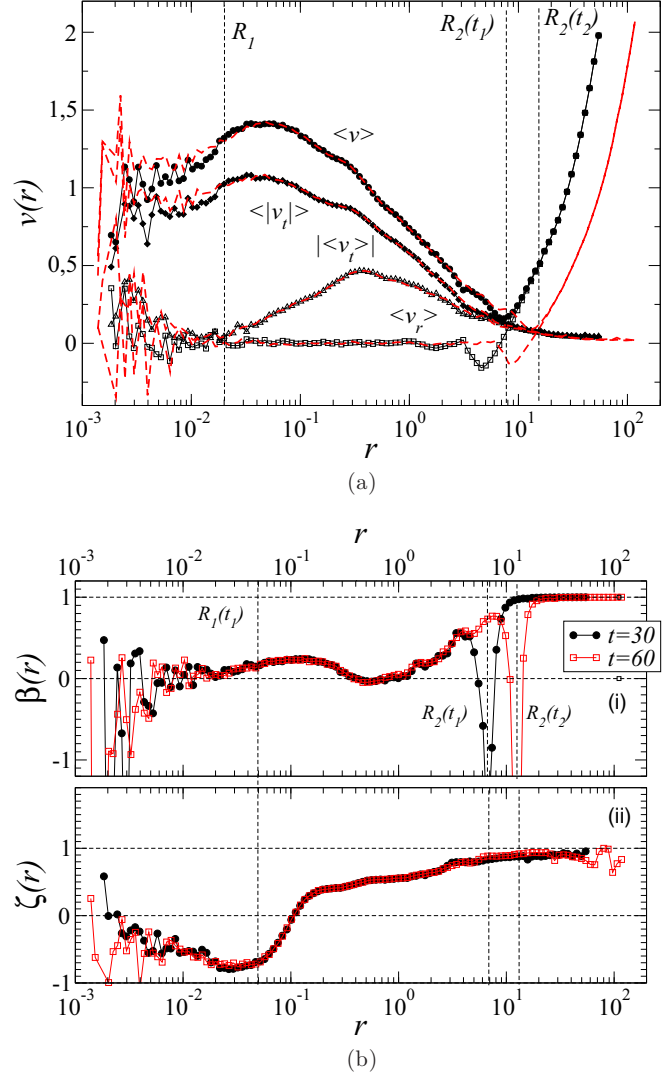


FIG. 6. Velocity field for run A1. (a) Particles' velocity and its components averaged in radial shells, as a function of radius, for two different times (symbols denote $t_1 = 30$ and lines $t_2 = 60$). (b) Functions (i) $\beta(r)$ and (ii) $\zeta(r)$ (see definitions in the legend) at two different indicated times.

this case the particles which arrive late during the collapse are those initially close to the outer shells of this plane of symmetry, and as they reexpand outward they give rise to a quite different spiral-like structure with flocculent multiple arms. These appear to be seeded by the growth of the density fluctuations in the system during its collapse phase; for this reason we expect that these features depend on the amplitude of the initial density fluctuations (see the discussion in Sec. III K). In addition, a transient ring structure emerges, which we discuss further below.

In B1, B1a, and B2 there is, because of the much more gentle collapse, very little or no ejected mass (for B1; see Fig. 7) and the motions are only predominantly radial at longer times and only at the very largest distances. Likewise, the region where the coherent rotational motion is dominant with respect to the radial motion is much more extended than for the case of, e.g., simulation A1. Differently from the other

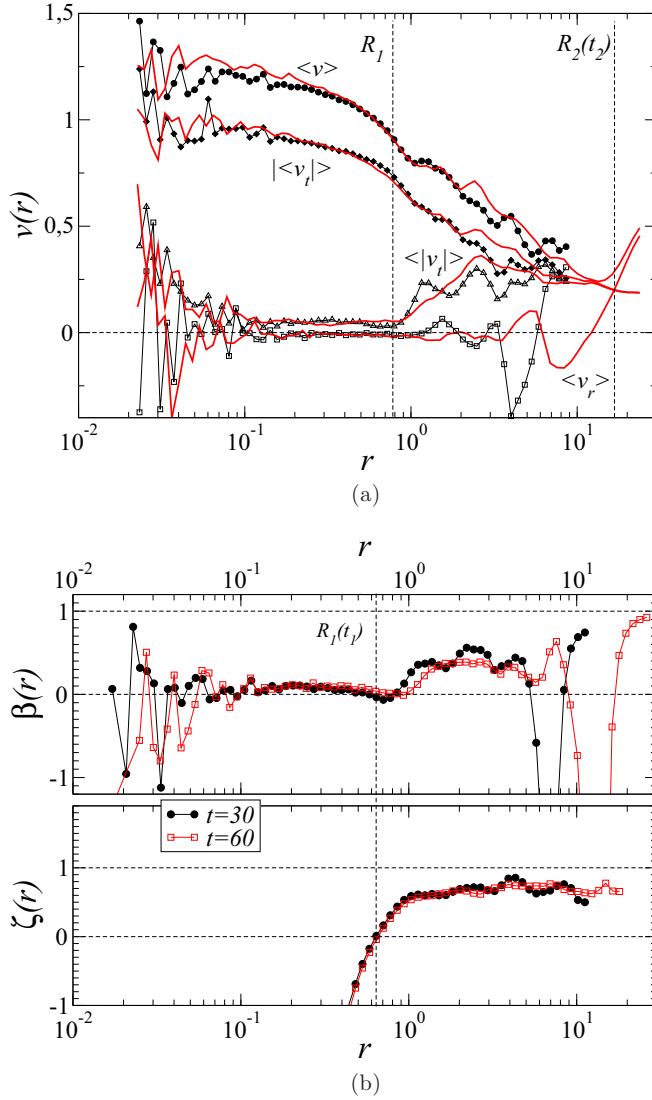


FIG. 7. Same as in Fig. 6 but for run B1.

cases, we observe in B2 that there appear to be two distinct phases in which we see quite different spiral arms emerge.

Simulations C1 and C2 show the typical behavior we observe in this class of more inhomogeneous and anisotropic ICs. Transient structures similar to those in the other cases again emerge and the same basic physical mechanism is at play. The spiral arm structure which forms after the collapse is clearly less axisymmetric, reflecting the lower symmetry of the IC. Both the visual appearance and the structure in velocity space (see Fig. 8) show that the resultant structures are more similar to A1 or A2 than to B1 or B2. This reflects the fact that the collapse is indeed stronger in these cases.

G. Formation of bar structures

We have noted that the structures we observe are generically nonaxisymmetric (except in specific cases like B2, where the axisymmetry of the IC survives the collapse phase better). Thus, not only is the configuration which results very flat along the axis parallel to the initially shortest semiprincipal axis, but a coherent anisotropic structure resembling a bar

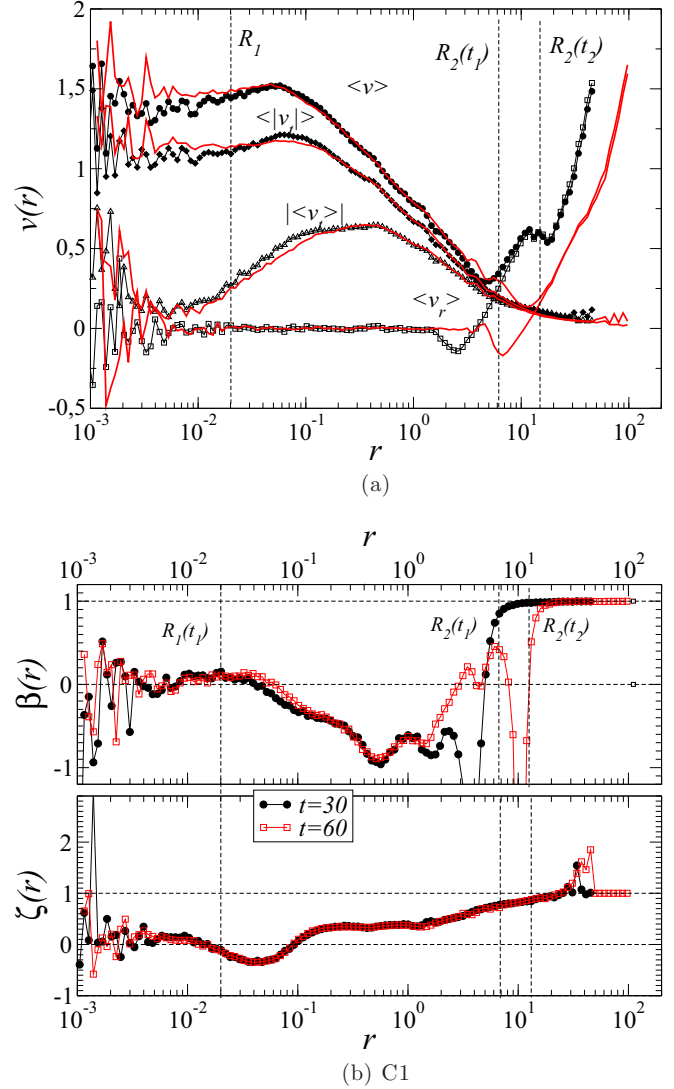


FIG. 8. Same as in Fig. 6 but for run C1.

emerges in the plane defined by the two longer semiprincipal axes in the IC. This anisotropy is, as one would anticipate, present not only in configuration space, but also in the velocity field.

Figure 9, showing several snapshots of B1 projected in the x - y plane, illustrates how these transient features form and grow. The particle distribution has been coarse grained onto a 32^3 grid and the average velocity determined in each cell. We see that, up to $t \approx 15$ when the global collapse of the system occurs, the velocities are essentially rotational, but progressively develop an inward radial component, simply because of the collapse dynamics. During the phase of maximal contraction, the particles originally farthest out, i.e., along the initial semiprincipal axis, gain a radial velocity component directed outward, but their total velocity remains predominantly rotational. The particles closer in initially, on the other hand, have lower energy and remain more bound around the central structure. Thus the two arms which emerge clearly are formed from two groups of particles which initially were located at opposite ends of the longest principal semiaxis. For longer

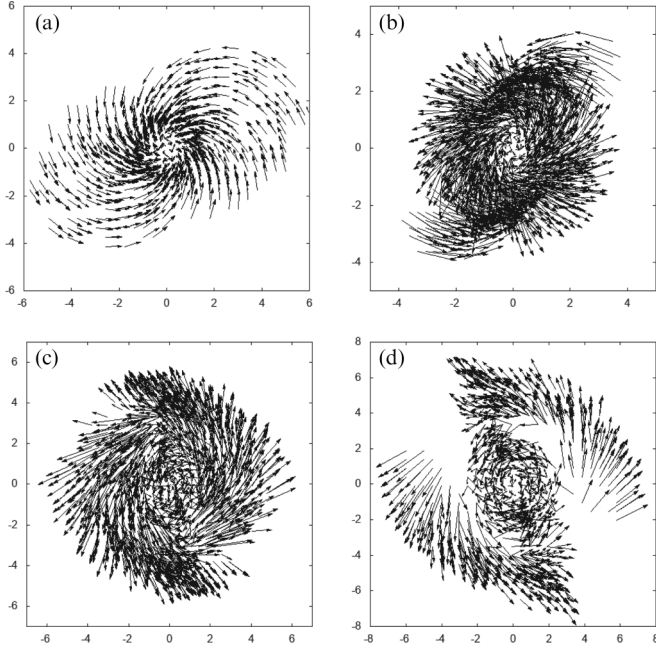


FIG. 9. Spatial evolution of B1 (coarse grained on a grid) on the x - y plane of the particles that form the bar or arm structures at $t = 25$. The times are (a) $t = 10$, (b) $t = 5$, (c) $t = 20$, and (d) $t = 5$. We have plotted the coarse-grained distribution (see the text) with the corresponding velocity vector.

timescales, i.e., $t > 50$, the spiral arms and the bar structure start to be washed out by the radial component of the motion.

H. Formation of ring structures

We have noted the formation of a time-dependent ringlike structure in simulation B2 at $t \approx 10$, in the plane corresponding to the two largest initial principal semiaxes. As can be seen in Fig. 10, this is indeed a local density enhancement which expands outward in time. Investigation confirms that it is generated by a fraction of particles moving outward at higher than average radial velocity. These are particles which were initially in or near the outermost radial shells in the plane of the oblate IC and which received a strong energy injection from the time-dependent potential generated by the collapse along the shortest axis. As these particles carry also the initial velocities of the rotation about this axis, the ring also rotates coherently. It persists up to the end of our simulation at $t = 50$. As noted, we have varied the ratios a_1/a_3 and a_2/a_3 , for the more general case of a triaxial ellipsoid, in a relatively wide range. We have found that, whenever we are close to an oblate ellipsoid, such a ringlike structure is formed.

I. Shape parameters

As we have discussed, the particles which gain the most energy are those which are initially farthest away from the center. For ICs like the ones we consider here, this leads to a very anisotropic distribution for the loosely bound and ejected mass. The details of this anisotropic distribution depend on the ICs. We recall that for cold prolate ellipsoidal ICs without rotation these particles are focused into two broad jets in

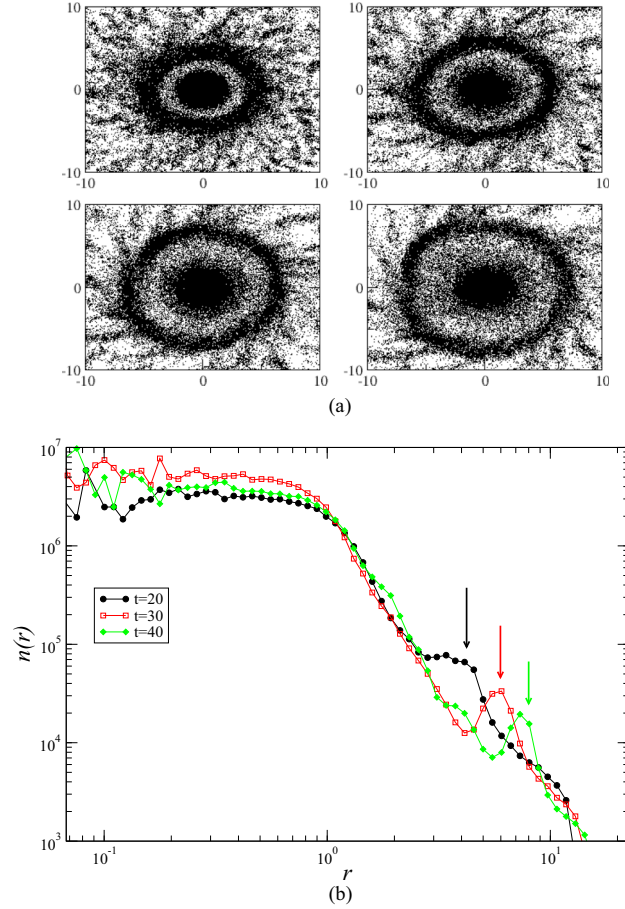


FIG. 10. (a) Close-up of the central part of simulation B2 (randomly sampled). (b) Evolution of the density profile of B2. The position of the expanding ring at different times (see the legend) is indicated by an arrow.

opposite directions around the initially longest semiprincipal axis [45]. This is the case simply because the particles farthest from the center are indeed close to this axis initially. With additional coherent rotation, as considered here, this jetlike structure is, as we have seen, transformed into a spiral-like structure as the particles propagate outward and the axis defined by the farthest out particles thus remains closely correlated with the initially longest semiprincipal axis.

In all our simulations the outer part of the structure is correspondingly very flat in the plane orthogonal to the initially shortest semiprincipal axis. Figure 11 shows the evolution of the three shape parameters ι , τ , and ϕ in simulation A1, separately for the internal particles constituting the core of the structure [Fig. 11(a)] and for the external particles constituting the spiral-like arms [Fig. 11(b)], where this division is defined by the radius at which the measured averaged radial density $n(r)$ discussed above reaches half its value in the core. In this case the core is a triaxial ellipsoid with $\iota \approx 0.3$, $\phi \approx 0.1$, and $\tau \approx 0.4$ and with $\iota \approx 0.7$, $\phi \approx 0.2$, and $\tau \approx 0.5$, respectively. On the other hand, the external particles are much more flat with $\iota \approx 3$, $\phi \approx 0.5$, and $\tau \approx 0.5$ in both cases.

A similar behavior is shown by the evolution of the flatness parameter for the simulations B1 and B2; in these cases ι is computed by considering only the external, low-energy,

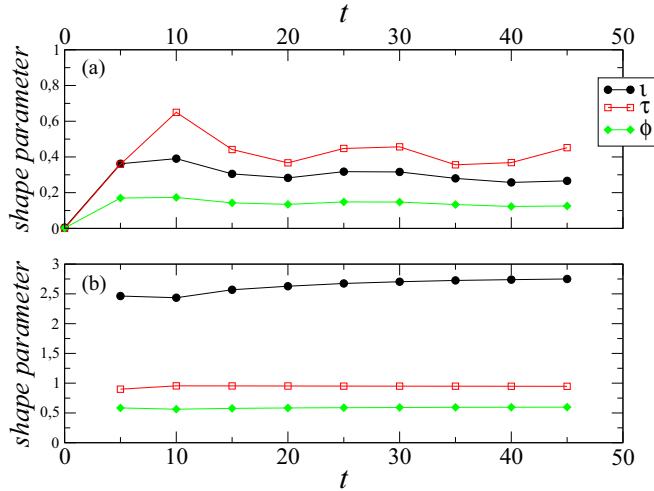


FIG. 11. Shape parameters for simulation A1: (a) internal particles and (b) external particles.

bound particles. In simulation B1, after the contraction phase during which ι is large and fluctuating, it becomes of order one for $t > 20$. In simulation B2, on the other hand, the flatness parameter remains of order one at all times without any significant variation. Simulations C1 and C2 are in this respect similar to A1 and A2.

J. Substructures

When the initial ellipsoidal deformation is large enough (e.g., $a_1/a_3 \approx 2$) the collapsing system may fragment into two or more clumps which eventually merge long after the collapse; this is the case of A2 (see Fig. 4). Clearly, when the IC is made up of clumps with small-amplitude fluctuations, as in C1 and C2, this effect is enhanced. On the other hand, during the collapse, initial density fluctuations may evolve due to gravitational instability forming small aggregates which, after the collapse, may correspond to substructures. These substructures, which are typically not virialized as they are subject to strong tidal fields, lie in the same plane defined by the jets. Eventually they will fall into the largest virialized object and be destroyed by the interaction with the core. The formation of substructures, anisotropically distributed on a planar configuration, around the main virialized object appears to be a generic result of the evolution from cold ICs of this type [45,46].

K. Role of density fluctuations and the continuum limit

Let us discuss further the role of density fluctuations in the collapsing cloud in an appropriate continuum limit defined by taking $N \rightarrow \infty$. How this limit is taken must be specified, as it is not unique. Indeed, here there are (at least) two evident ways of taking such a limit, and the role of density fluctuations is different in each case.

First, if we consider finite- N configurations as Poisson samplings of continuum configurations with fixed mass density ρ_0 , i.e., without any intrinsic density fluctuations, we can take the limit $N \rightarrow \infty$ together with the particle mass $m \rightarrow 0$ so that $\rho_0 = N \times m = \text{const}$. In this case the density

fluctuations, which are proportional in amplitude to $\delta\rho/\rho_0 \propto N^{-1/2}$, also vanish. In this case all substructures generated by the growth of density fluctuations must disappear in the continuum limit. They can in this sense then be interpreted as finite- N effects.

On the other hand, we can also take the continuum limit in a different way, by taking $N \rightarrow \infty$ and $m \rightarrow 0$ with $\rho_0 = N \times m = \text{const}$ and with $\delta\rho/\rho_0 = \text{const}$ (or, more precisely, keeping the statistical properties of the latter fixed); in this case the internal fluctuations of the cloud grow in the same way independently of N and thus they give rise to the same substructures. Indeed, as it was shown in detail in [33] for the case of the spherical collapse model, while the whole system collapses small density fluctuations inside the cloud grow and form substructures of increasing size with time. The collapse is halted when the size of nonlinear structures formed inside the collapsing cloud becomes of the same order of magnitude as the cloud itself (which meanwhile is collapsing). Thus, in this process there are two competing effects: the global monolithic collapse, which is a top-down process, and the bottom-up mechanism of structure formation. This latter mechanism is regulated by the properties of density fluctuations (in our case a simple Poisson distribution).

As final remark we note that the question of how many particles are in practice needed to simulate accurately the collisionless limit (up to some specified time) can only be answered in the context of a given problem and it is in general a very difficult task to sort out. For instance, it was recently shown through the study of the evolution a simple class of initial conditions (initially spherical density profiles) that there is a distinct N dependence associated with the presence of instabilities in the collisionless dynamics that arises because the initial seeds for the instability themselves depend on N [43]; this dependence on N is very difficult to find, as it manifests itself only in a very weak dependence of the time of triggering of the instability and not, at sufficiently large N , in the properties of the state to which the instability drives the system.

The continuum limit for the dynamics of our finite- N systems is given by the Vlasov-Poisson system and in principle could be simulated numerically directly. While much progress has been made on the numerical solution of these equation (see, e.g., [47]), such an approach is, for the present, feasible numerically only for systems with high degrees of symmetry and not for those here in which the breaking notably of rotational symmetry plays a crucial role.

IV. MODELS AND OBSERVED STRUCTURES

Both our initial conditions and the dynamics of the systems we are studying are highly idealized. In particular, we expect that in the formation of most astrophysical structures nongravitational processes will play a crucial role (e.g., gas dynamics, star formation, and feedback from it in galaxy formation). Thus our models are intrinsically not suitable to provide a detailed quantitative model for the formation of astrophysical objects. On the other hand, focusing on the specific case of galaxy formation, we note that there is in fact little direct constraint on initial conditions for it, as the fluctuations measured in the cosmic microwave background constrain strongly only

significantly larger scales. Further, the relative importance of gravity and other forces in shaping galaxies is very uncertain. As the structures we have seen in our simulations bear a striking resemblance to spiral galaxies, we believe it is worth looking more carefully at whether the qualitative features of these structures are compatible or incompatible with the observed qualitative properties of galaxies.

A. Morphological features

First we note that there are several very common and nontrivial features of spiral galaxies, which are accounted for in this kind of model while they are problematic in the usual theoretical approaches, in which spiral structures emerge through instability of an equilibrium disk (see, e.g., [14,15]). Our models lead, as we have seen, very easily to a two-armed spiral structure, which is observationally the most common kind. Its predominance has been considered puzzling and is difficult to account for in the usual theoretical approaches. Further, the pitch angle α , defined as the angle between the tangent to the arm and the tangent to a circle at the same angle, gives values in the range 10° – 40° in our simulations (at $t = 50$) except for the very cold cases like A1, in which the particles are ejected with very high radial velocities (leading to an α approaching 90°). Pitch angles of this order are typical observationally, while theoretical models predict much smaller angles and have great difficulty accounting for those observed [15]. Further, as is almost invariably the case observationally, the spiral arms formed in our models are trailing, i.e., the outer tip points in the direction opposite to rotation [14]. As we have described above, the spiral-like structure arises precisely because the particles which are farthest out have, by angular momentum conservation, smaller transverse velocities and thus lag behind in the angle they rotate through up to a given time. This is again an observational fact which does not have an apparent explanation in the usual theoretical approaches. Finally, our mechanism produces, by construction, structures which are nonaxisymmetric and often the central core is barlike. Further, the spiral arms start at the end of the bar. These properties likewise appear not only to be compatible with observations (see, e.g., [15,48]), but to potentially explain them in a very natural manner which eludes the usual theoretical approaches.

Finally, it is interesting to note that the mass of stars and gas in the spiral arms and in the outer part of the disk in general do not exceed the $\sim 20\%$ of the luminous mass of the galaxy (see, e.g., [49]). In our simulations we also find that most of the mass is concentrated in the central bulge and that the fraction of particles with energy close to or larger than zero represents a small fraction, typically of the order of 10% – 20% , of the total mass.

B. Timescales

We have discussed in [36] some simple considerations about the compatibility of timescales and length scales with real spiral galaxies, for the most idealized case of a single ellipsoidal cloud. Making simple assumptions linking the final size and velocity scale to those of real galaxies, the collapse process which generated the structure must be assumed to

occur on a timescale of the order of ~ 1 Gyr, which is the characteristic timescale of all out-of-equilibrium transient structures that are formed in our simulations, i.e., spiral arms, bars, and ringlike structures. This is much shorter than the age of the oldest stars in these galaxies (~ 10 Gyr), which is usually assumed to correspond also to the age of such structures. From the observational point of view, however, there is no definitive evidence establishing the age of spiral arms; rather some observations have suggested that spiral arms are not long-lived (see, e.g., [14,15] and references therein). Indeed, the oldest stars and the galaxy are formed by very different dynamical processes occurring on very different length scales [the size of the clouds where star formation occurs is of the order of 10^{-2} – 10^{-1} kiloparsec (kpc), while the size of a typical galaxy is 10 – 10^2 kpc] and thus it is not at all evident that these two timescales must be of the same order of magnitude.

The second family of ICs we have studied here illustrates clearly that this timescale inferred from the space and velocity scales represent only that of the violent collapse leading to this outer structure, which could quite possibly be dissociated from that of the formation of the central part of the galaxy, which could occur much before a secondary collapse of surrounding matter, giving rise to the disk and extended halo structure we have described. In this respect it is perhaps useful to recall that the usual assumption in modeling galaxies as dynamical equilibria (i.e., as QSSs) is intimately linked to these considerations of timescales and length scales. Indeed, if we suppose a star orbits the galactic centers at a distance R , the number of revolutions it has made in a time T is

$$n_{\text{rev}} = \frac{T}{2\pi R/v} \approx 30 \frac{T_{10} v_{200}}{R_{10}}, \quad (14)$$

where T_{10} is the timescale in units of 10 Gyr, v_{200} is the velocity in units of $v = 200$ km/s, and R_{10} is the radius in units of 10 kpc.

For stars (or other emitters) moving on closed Keplerian orbits, with a circular velocity $v \sim \sqrt{GM/r}$, this assumption (of stationarity) appears to be reasonable only if $n_{\text{rev}} \gg 1$, i.e., if these bodies have characteristic crossing times in the system considerably longer than its estimated lifetime. For smaller values they cannot have had the time to attain orbits in which there is an equilibrium between centrifugal and centripetal acceleration. The precise value of the number of revolutions needed to reach a relaxed configuration cannot be constrained in a simple way theoretically because, as we have discussed above, it depends on the time in which the relaxation from an out-of-equilibrium configuration to a QSS takes place. However, from a qualitative point of view, a reasonable requirement is that $n_{\text{rev}} \gg 1$; only if this condition is satisfied can the assumption of stationarity possibly be justified.

For a typical disk galaxy of the size of the Milky Way, with a characteristic velocity $v_{200} \sim 1$, the number of revolutions is $n_{\text{rev}} \geq 10$ for $R \leq 30$ kpc only if $T_{10} \sim 1$, i.e., if the age of the galaxy structure is of order of the oldest stars. If $T_{10} \sim 1$, i.e., if the age of the galaxy structure is of order of the oldest stars, then objects in the inner part of the galaxy (i.e., $R < 10$ kpc) have enough time to make $n_{\text{rev}} \geq 10^2$, while at larger distances $n_{\text{rev}} \leq 10$ and thus the assumption that emitters move on closed Keplerian orbits appears very difficult to justify for

the outermost regions of the galaxy. On the other hand, if the age of the galaxy structure is $T_{10} \sim 0.1$, the assumption of stationarity clearly cannot be valid at larger radii because $n_{\text{rev}} \ll 10$. The out-of-equilibrium scenario of our models for the outer parts of a galaxy of the size of the Milky Way, however, is then coherent with the observed velocity and distance scales.

C. Velocities

The compatibility of the velocity space structure of our transient structures with observed properties of galaxies is much less evident. Indeed, a generic feature of the structures in our simulations, arising from the nature of the mechanism, is that velocities becomes predominantly radial at large radii. Extensive observational study over decades, using different tracers, has placed much constraint on such motions [49] and indicates that motion in the outer parts of such galaxies is in fact predominantly rotational [49,50], although significant radial motions have been detected in many objects [51]. As discussed in [36] for the results based on simple ellipsoidal ICs, it turns out that the naive expectation that such motions are excluded by observations is not confirmed. The reason is that our velocity fields have a very particular (anisotropic) spatial structure, which makes it difficult to distinguish them in projection from rotating disk models. For the broader class of ICs we have explored here, the same considerations are valid, as there is a similar kind of correlation between the velocities and the spatial configuration. Further, we have seen that different ICs can produce a less violent evolution than in the pure ellipsoidal model, leading to less radial motion and a much more extended region in which there is predominantly rotational motion. Thus the compatibility with observations of galaxy kinematics depends also on the identification of the timescales and length scales of the models with those of real galaxies. In our conclusion below we will comment about the radial motions observed in our own galactic disk, which are relevant to understand the possible nonstationary nature of the outer parts of the disk and of the spiral arms.

V. DISSIPATIONLESS AND DISSIPATIVE DISK FORMATION

Let us now briefly discuss the difference between the models that we have presented, where the formation of a disklike flat structure is originated solely by a gravitational, and thus dissipationless, dynamics and models in which instead the formation of a disklike structure is driven by dissipative effects. In standard models of galaxy formation the key element in the formation of a disk galaxy is the dissipation associated with nongravitational processes: gas dynamics, cooling, star formation, etc. The models used when gas dynamics is added to gravitational physics consider the collapse of isolated and rotating clouds, like the one we studied here, but solely with a spherical initial configuration. The central finding of our study is that disklike configurations with transient spiral arms and with bars and/or rings in our simulations are formed by a purely dissipationless gravitational dynamics if the initial conditions break spherical symmetry. There have been attempts [18] to study the formation of quasiequilibrium configurations

through a purely gravitational and dissipationless collapse dynamics in which the initial conditions are represented by isolated, spherically symmetric top hats in solid-body rotation and in Hubble flow. These initial conditions differ from the ones we considered in this work by (i) the initial spherical shape and (ii) the small-scale fluctuations, intended to model the fluctuations in standard cold dark-matter cosmologies. Starting from these initial conditions, the QSSs formed are slowly rotating, are supported by an anisotropic velocity dispersion, closely resemble elliptical galaxies, and do not resemble at all spiral galaxies.

The seminal work in [16] described a scenario (then developed in many other subsequent works) in which elliptical galaxies are products of a purely gravitational dissipationless collapse at high redshift, while spirals formed later with considerable dissipation. To simulate such a scenario, dissipative gas dynamics was included in numerical simulations [19] in a system with the same class of initial conditions as in [18]. It is precisely the dynamics of the gas in this two-component system which leads then to structures resembling spiral galaxies: a thin disk made of gas and surrounded by purely gravitational matter. Indeed, since the gas can shock and dissipate energy it can develop a much flatter distribution than the dissipationless matter. By adding to the same initial conditions of [18] other nongravitational effects such as star formation, supernova feedback [20], and metal enrichment due to supernovae [21,22], the crucial mechanism for the formation of the disk and of spiral arms is again played by dissipative nongravitational processes. These scenarios are thus completely different in how this structure emerges in our simulations, which are pure gravitational and dissipationless.

VI. DISCUSSION AND CONCLUSIONS

We have described the results of numerical experiments exploring the evolution under their self-gravity of nonspherical uniform and nonuniform clouds with a coherent rigid-body rotation about their shortest semiprincipal axis. We have focused in particular on the very rich spatial and velocity space organization of the outer parts of these structures, which is a result of the combination of the violent relaxation, which leads to a high-energy tail in the energy distribution, and the coherent rotation. Under very general conditions spiral-like structure arises, while more or less evident bars and/or rings appear depending on the properties of the initial conditions. These outer parts of the structure are intrinsically nonstationary and continue indefinitely to evolve in time. Although it will disappear asymptotically, such structure is very long lived and, in most cases, is still clearly defined at the longest times we simulate to, of order 100–200 times the dynamical time (characterizing the time for the formation and the characteristic time of the virialized core). The particles forming the spiral arms will escape from the system, if they have positive energy, or will form an extremely dilute and anisotropic halo; eventually some of them, those having negative energy, will return toward the core. On the other hand, the largest fraction of the mass is bound in a triaxial system.

It is perhaps relevant to remark why this simple path to producing such a structure in a self-gravitating system has apparently been overlooked in the literature. Indeed, the

dynamics of self-gravitating clouds of various forms and with a wide variety of initial velocity distributions, with and without initial angular momentum, has been studied in depth in the literature and it may seem surprising that the phenomena we have discussed have not been noticed. We believe that the explanation is probably linked to, on the one hand, the small fraction of mass involved and, on the other hand, the relatively long timescales on which the system must be monitored. Indeed, most studies of this kind of system focus on the relatively short times on which the system appears to virialize as indicated by global parameters. Further, most studies of this kind date back two to three decades and include simulations in which the number of particles was typically of $\sim 10^4$. In this case, the high-energy particles which are typically of order 5%–10% are too few to resolve the structures we have studied.

The spatial distributions of these transient structures are all spiral-like, but even within the very circumscribed and idealized set of ICs we have considered, they show a wide variety of forms, from ones qualitatively resembling grand design spiral galaxies to multiarmed and flocculent spiral galaxies and barred spiral galaxies. The mechanism for producing these structures is completely different in its physical principle from the mechanisms widely considered as potentially explaining observed spiral structure. Indeed, while such mechanisms treat the spiral structure as a perturbative phenomenon, produced by the perturbation of an equilibrium rotating disk [14,15,52–56], the mechanism at play in our simulations is intrinsically far out of equilibrium. While our model is too simple and idealized to provide a quantitative model for real spiral galaxies, we have noted that, in many respects, it apparently reproduces very naturally many of their noted qualitative features.

For what concerns the problem of cosmological galaxy formation, we note that the monolithic collapse discussed here is compatible with a top-down structure formation of the kind that occurs, e.g., in the so-called warm dark-matter models. On the other hand, in models where dark matter is cold, structure formation proceeds in a hierarchical bottom-up manner so that galaxies are formed through an aggregation (i.e., merging) of smaller substructures. In this respect we note that when the initial conditions break spherical symmetry and are inhomogeneous (as for our models C1 and C2), before the complete monolithic collapse of the whole cloud there are substructures forming and merging; in this scenario, because all substructures take part in the whole system's collective dynamics, they can finally form coherent structures, like bars, rings, and spiral arms, which are as large as the system itself. Thus, the scenario we have discussed is not in contradiction with the various observational evidence that merging was efficient in the early universe, but clearly a comprehensive theory of cosmological structure formation must be specified by the whole power spectrum of density fluctuations; however, this is beyond the scope of the present work.

We will leave for future work some of the questions opened up by our results. One such question is of course whether the kind of initial conditions we assume could be produced easily within a cosmological framework. As mentioned above, the problem of collapsing clouds has been widely studied in the context of cosmological galaxy formation; however, these studies were performed by taking a spherical overdensity, while we used here more general shapes and a purely gravitational (and thus dissipationless) dynamics. In addition, we note that while this seems to be excluded in typical scenarios in which structure formation proceeds hierarchically from very small scales (e.g., cold dark-matter-type scenarios), conditions like those we assume might possibly be plausible in the case in which initial fluctuations are highly suppressed below some large scale (e.g., as occurs in warm dark-matter-type scenarios). A different but complementary direction would be to explore the additional effects of nongravitational and dissipative physics, like gas dynamics, modeling the complex processes inevitably at play in galaxy formation, and how they may or may not modify the formation and evolution of the structures we have focused on here.

Finally, it is interesting to mention that, while it has been known for several decades that the disk of the Milky Way contains large-scale nonaxisymmetric features, the full knowledge of these asymmetric structures and of their velocities fields is still lacking. The recent Gaia DR2 maps [57] have clearly shown that the Milky Way is not, even to a first approximation, an axisymmetric system at equilibrium, but that it is characterized by streaming motions in all three velocity components. In particular, it has confirmed the coherent radial motion in the direction of the anticenter, detected earlier in [51], up to 14 kpc. In addition, recent analyses of the radial velocity field in our galaxy by using different data sets [58,59] provide a great deal of different and corroborated information about the disk kinematics of our galaxy: significant departures of circularity in the mean orbits with radial galactocentric velocities, variations of rotation speed with position, asymmetries between northern and southern galactic hemisphere, etc. (note that the analysis of the velocity fields in external galaxies is model dependent and thus so is the estimation of radial motions [60]). These features of the full three-dimensional velocity field seem to be compatible with the complex velocity fields generated by the gravitational collapses we have discussed, but a more detailed comparison of the models and observations is needed.

ACKNOWLEDGMENTS

This work was granted access to the HPC resources of The Institute for Scientific Computing and Simulation financed by Region Ile de France and the project Equip@Meso (Reference No. ANR-10-EQPX-29-01) overseen by the French National Research Agency as part of the Investissements d'Avenir program. F.S.L. thanks Martin López-Corredoira for very useful discussions and comments.

[1] A. Campa, T. Dauxois, D. Fanelli, and S. Ruffo, *Physics of Long-Range Interacting Systems* (Oxford University Press, Oxford, 2014).

[2] P.-H. Chavanis, *Astron. Astrophys.* **556**, A93 (2013).

[3] Y. Levin, R. Pakter, F. B. Rizzato, T. N. Teles, and F. P. Benetti, *Phys. Rep.* **535**, 1 (2014).

- [4] T. Padmanabhan, *Phys. Rep.* **188**, 285 (1990).
- [5] P.-H. Chavanis, C. Rosier, and C. Sire, *Phys. Rev. E* **66**, 036105 (2002).
- [6] T. Dauxois, S. Ruffo, E. Arimondo, and M. Wilkens, *Dynamics and Thermodynamics of Systems with Long Range Interactions* (Springer, Berlin, 2002).
- [7] Y. Y. Yamaguchi, J. Barré, F. Bouchet, T. Dauxois, and S. Ruffo, *Physica A* **337**, 36 (2004).
- [8] A. Campa, T. Dauxois, and S. Ruffo, *Phys. Rep.* **480**, 57 (2009).
- [9] M. Joyce and T. Worrakitpoonpon, *J. Stat. Mech.* (2010) P10012.
- [10] B. Marcos, *Phys. Rev. E* **88**, 032112 (2013).
- [11] F. P. C. Benetti, A. C. Ribeiro-Teixeira, R. Pakter, and Y. Levin, *Phys. Rev. Lett.* **113**, 100602 (2014).
- [12] B. Marcos, A. Gabrielli, and M. Joyce, *Phys. Rev. E* **96**, 032102 (2017).
- [13] S. Chandrasekhar, *Rev. Mod. Phys.* **15**, 1 (1943).
- [14] J. Binney and S. Tremaine, *Galactic Dynamics* (Princeton University Press, Princeton, 2008).
- [15] C. Dobbs and J. Baba, *Pub. Astron. Soc. Austr.* **31**, e035 (2014).
- [16] J. R. Gott III, *Annu. Rev. Astron. Astrophys.* **15**, 235 (1977).
- [17] G. Lake and R. G. Carlberg, *Astron. J.* **96**, 1581 (1988).
- [18] N. Katz, *Astrophys. J.* **368**, 325 (1991).
- [19] N. Katz and J. E. Gunn, *Astrophys. J.* **377**, 365 (1991).
- [20] N. Katz, *Astrophys. J.* **391**, 502 (1992).
- [21] M. Steinmetz and E. Müller, *Astron. Astrophys.* **281**, L97 (1994).
- [22] M. Steinmetz and E. Müller, *Mon. Not. R. Astron. Soc.* **276**, 549 (1995).
- [23] F. Marinacci, R. Pakmor, and V. Springel, *Mon. Not. R. Astron. Soc.* **437**, 1750 (2014).
- [24] T. Naab and J. P. Ostriker, *Annu. Rev. Astron. Astrophys.* **55**, 59 (2017).
- [25] M. Henon, *Ann. Astrophys.* **24**, 229 (1973).
- [26] T. van Albada, *Mon. Not. R. Astron. Soc.* **201**, 939 (1982).
- [27] S. Aarseth, D. Lin, and J. Papaloizou, *Astrophys. J.* **324**, 288 (1988).
- [28] M. David and T. Theuns, *Mon. Not. R. Astron. Soc.* **240**, 957 (1989).
- [29] L. Aguilar and D. Merritt, *Astrophys. J.* **354**, 73 (1990).
- [30] T. Theuns and M. David, *Astrophys. Space Sci.* **170**, 267 (1990).
- [31] C. Boily, E. Athanassoula, and P. Kroupa, *Mon. Not. R. Astron. Soc.* **332**, 971 (2002).
- [32] E. I. Barnes, P. A. Lanzel, and L. L. R. Williams, *Astrophys. J.* **704**, 372 (2009).
- [33] M. Joyce, B. Marcos, and F. S. Labini, *Mon. Not. R. Astron. Soc.* **397**, 775 (2009).
- [34] F. S. Labini, *Mon. Not. R. Astron. Soc.* **423**, 1610 (2012).
- [35] F. S. Labini, *Mon. Not. R. Astron. Soc.* **429**, 679 (2013).
- [36] D. Benhaiem, M. Joyce, and F. S. Labini, *Astrophys. J.* **851**, 19 (2017).
- [37] V. Springel, *Mon. Not. R. Astron. Soc.* **364**, 1105 (2005).
- [38] V. Springel, User guide for GADGET-2, available at <https://www.mpa.mpg.de/gadget/users-guide.pdf> (2005).
- [39] P. J. E. Peebles, *Astrophys. J.* **155**, 393 (1969).
- [40] P. J. E. Peebles, *Astron. Astrophys.* **11**, 377 (1971).
- [41] J. Barnes and G. Efstathiou, *Astrophys. J.* **319**, 575 (1987).
- [42] J. S. Bullock, A. Dekel, T. S. Kolatt, A. V. Kravtsov, A. A. Klypin, C. Porciani, and J. R. Primack, *Astrophys. J.* **555**, 240 (2001).
- [43] D. Benhaiem, M. Joyce, F. S. Labini, and T. Worrakitpoonpon, *Mon. Not. R. Astron. Soc.* **473**, 2348 (2018).
- [44] C. C. Lin, L. Mestel, and F. H. Shu, *Astrophys. J.* **142**, 1431 (1965).
- [45] D. Benhaiem and F. S. Labini, *Mon. Not. R. Astron. Soc.* **448**, 2634 (2015).
- [46] D. Benhaiem and F. S. Labini, *Astron. Astrophys.* **598**, A95 (2017).
- [47] T. Sousbie and S. Colombi, *J. Comput. Phys.* **321**, 644 (2016).
- [48] C. J. Jog and F. Combes, *Phys. Rep.* **471**, 75 (2009).
- [49] Y. Sofue, *Pub. Astron. Soc. Jap.* **69**, R1 (2017).
- [50] P. M. W. Kalberla and L. Dedes, *Astron. Astrophys.* **487**, 951 (2008).
- [51] M. López-Corredoira and C. González-Fernández, *Astron. J.* **151**, 165 (2016).
- [52] F. Hohl, *Astrophys. J.* **168**, 343 (1971).
- [53] T. A. Zang and F. Hohl, *Astrophys. J.* **226**, 521 (1978).
- [54] J. A. Sellwood, *Mon. Not. R. Astron. Soc.* **217**, 127 (1985).
- [55] J. A. Sellwood and E. M. Moore, *Astrophys. J.* **510**, 125 (1999).
- [56] M. S. Fujii, J. Baba, T. R. Saitoh, J. Makino, E. Kokubo, and K. Wada, *Astrophys. J.* **730**, 109 (2011).
- [57] Gaia Collaboration, D. Katz, T. Antoja, M. Romero-Gómez, R. Drimmel, C. Reylé, G. M. Seabroke, C. Soubiran, C. Babusiaux, P. Di Matteo *et al.*, *Astron. Astrophys.* **616**, A11 (2018).
- [58] M. López-Corredoira, F. S. Labini, P. M. W. Kalberla, and C. A. Prieto, *Astron. J.* **157**, 26 (2019).
- [59] M. López-Corredoira and F. S. Labini, *Astron. Astrophys.* **621**, A48 (2019).
- [60] F. S. Labini, D. Benhaiem, S. C. Omerón, and M. López-Corredoira, *Astron. Astrophys.* **622**, A58 (2019).